

Aeroelastic Analysis of Aircraft Wind-Tunnel Model Coupling Structural and Fluid Dynamic Codes

Ubaldo Cella*

Piaggio Aero Industries, 80078 Naples, Italy

and

Marco Evangelos Biancolini†

University of Rome “Tor Vergata”, 00133 Rome, Italy

DOI: 10.2514/1.C031293

A procedure coupling Reynold-averaged Navier–Stokes computation and finite element method analysis based on the use of radial basis functions has been set up and validated against experimental data. A static fluid–structure simulation on a complete aircraft configuration has been performed coupling high-fidelity methods. The analysis was performed on a wind-tunnel aircraft model in high-speed configuration using the commercial CFD++ Navier–Stokes code and the Nastran structural analysis code. The mesh morphing tool RBF-Morph and load interpolation procedures were applied to couple the two solutions. The results of the analysis were validated against Piaggio Aero Industries property high-speed experimental data, obtained during a test campaign performed in the ONERA S2MA transonic wind tunnel.

I. Introduction

THE interest in developing a multidisciplinary approach using high-fidelity numerical analysis methods is today, in the aeronautical field, strongly increasing. The capability to couple accurate methods able to model the physics of the several aspects of the design and their interaction is increasing the accuracy of the numerical analysis, improving (as a consequence) the designer capability to produce higher-performance products. This is particularly true with the vision of modern design methods, which are today strongly oriented on the application of numerical optimization procedures.

In aerodynamics, the fluid–structure interaction is, in most of the cases, a mechanism that cannot be neglected. For this reason, big efforts have been addressed on this topic during the last decade. In [1], the study of a complete aircraft accounting for fluid–structure interaction in flight conditions is presented. The method of radial basis functions (RBFs) is here used for updating the computational fluid dynamics (CFD) mesh in the deformed shape calculated using the finite element method (FEM). The great potential of RBFs in this field has been previously demonstrated in [2], where the same method is used to parameterize and optimize the shape of a wing, in [3], where the RBF method is used as a shape parameterization tool, and in [4], where a simple fluid–structure application is presented using RBFs and modal superposition. Past applications of fluid–structure interaction for practical industrial problems were presented in the past by the authors [5–8]. In [5], an implementation using the commercial Fluent solver and a custom FEM solver for beam structures has been presented, and the method has been then presented in [6], showing very good agreement with respect to experiments for two-dimensional flow problems (a reed valve and an elastic dam). The method has been extended to three-dimensional problems using Fluent and an embedded structural solver that uses mass and stiffness matrixes generated by the commercial FEM solver Nastran [7]; here, a formula 1 front wing study has been faced,

accounting for transient structural deformations. A custom shell element was then introduced to manage arbitrary problems (both linear and nonlinear, using implicit and explicit approaches for the structural study); an example about a six-petal reed valve is demonstrated in [8], and the same approach was successfully used for the simulation of the movement of a sheet of paper in a printing device.

Recently, the use of RBFs for shape parameterization of large industrial problems was demonstrated in [9,10], showing how such technology can be used for the shape optimization of a motorbike deflector using the software tool RBF-Morph;‡ a detailed description of the tool and its application is included in [11]. Details about the use of such a tool for fluid–structure interaction problems are provided in [12].

The present paper describes a CFD–computational structural mechanics (CSM) procedure that has been set up with the aim to perform a static aeroelastic analysis (unsteady phenomena, such as flutter or buffeting, were not investigated in this work but are subjects of ongoing research). The commercial CFD++ Navier–Stokes code has been coupled with the NASTRAN FEM analysis code. The code solutions have been linked, applying the mesh morphing tool RBF-Morph. The aerodynamic wing load has been applied to the non-conformal structural mesh by a Patran interpolating procedure. The FEM grid point displacement solution has then been used to morph the grid and to prosecute with a new aerodynamic analysis on the deformed geometry.

II. Theoretical Background

A system of radial functions is used to produce a solution for mesh movement/morphing from a list of source points and their displacements. This approach is valid for both surface shape changes and volume mesh smoothing.

Radial bases were born as an interpolation tool for scattered data and consist of a very powerful tool because they are able to interpolate everywhere in the space a function defined at discrete points giving the exact value at original points. The behavior of the function between points depends on the kind of basis adopted.

The radial function can be fully or compactly supported; in any case, a polynomial corrector is added to guarantee compatibility for rigid modes. Typical radial functions are reported in Table 1.

Received 3 November 2010; revision received 30 July 2011; accepted for publication 28 August 2011. Copyright © 2011 by the American Institute of Aeronautics and Astronautics, Inc. All rights reserved. Copies of this paper may be made for personal or internal use, on condition that the copier pay the \$10.00 per-copy fee to the Copyright Clearance Center, Inc., 222 Rosewood Drive, Danvers, MA 01923; include the code 0021-8669/12 and \$10.00 in correspondence with the CCC.

*Senior Research Engineer, Piaggio High Technology, Via Campi Flegrei 34, Pozzuoli.

†Researcher, Department of Mechanical Engineering, Via del Politecnico 1.

‡Data available at <http://www.rbf-morph.com/> [retrieved 18 February 2011].

Table 1 RBFs

RBF	$\phi(r)$
Spline type (R_n)	$ r ^n, n \text{ odd}$
Thin plate spline (TPS _n)	$ r ^n \log r , n \text{ even}$
Multiquadric	$\sqrt{1+r^2}$
Inverse multiquadric	$\frac{1}{\sqrt{1+r^2}}$
Inverse quadratic	$\frac{1}{1+r^2}$
Gaussian	e^{-r^2}

As will be shown in detail, a linear system (of order equal to the number of source points introduced) needs to be solved for coefficient calculation. Once the unknown coefficients are calculated, the motion of an arbitrary point inside or outside the domain (interpolation/extrapolation) is expressed as the summation of the radial contribution of each source point (if the point falls inside the influence domain). Details of the theory need to be given using some equations. An interpolation function composed by a radial basis and a polynomial is defined as follows:

$$s(\mathbf{x}) = \sum_{i=1}^N \gamma_i \phi(\|\mathbf{x} - \mathbf{x}_i\|) + h(\mathbf{x})$$

The degree of the polynomial has to be chosen depending on the kind of radial function adopted. A radial basis fit exists if the coefficients γ and the weight of the polynomial can be found such that the desired function values are obtained at source points and the polynomial terms gives zero contributions at the source points; that is,

$$s(\mathbf{x}_{k_i}) = g(\mathbf{x}_{k_i}) \quad 1 \leq i \leq N$$

$$0 = \sum_{i=1}^N \gamma_i q(\mathbf{x}_{k_i})$$

for all polynomials q with a degree less than or equal to that of polynomial h . The minimal degree of polynomial h depends on the choice of the basis function. A unique interpolant exists if the basis function is a conditionally positive definite function. If the basis functions are conditionally positive definite of order $m = 2$, a linear polynomial can be used:

$$h(\mathbf{x}) = \beta + \beta_1 x + \beta_3 y + \beta_4 z$$

The subsequent exposition will assume valid the aforementioned hypothesis. A consequence of using a linear polynomial is that rigid body translations are exactly recovered. The values for the coefficients γ of RBF and the coefficients β of the linear polynomial can be obtained by solving the system

$$\begin{pmatrix} \mathbf{M} & \mathbf{P} \\ \mathbf{P}^T & \mathbf{0} \end{pmatrix} \begin{pmatrix} \gamma \\ \beta \end{pmatrix} = \begin{pmatrix} \mathbf{g} \\ \mathbf{0} \end{pmatrix}$$

where g are the known values at the source points. M is the interpolation matrix defined calculating all the radial interactions between source points

$$M_{ij} = \phi(\|\mathbf{x}_{k_i} - \mathbf{x}_{k_j}\|) \quad 1 \leq i \leq N$$

and P is a constraint matrix that arises, balancing the polynomial contribution, and contains a column of 1s and the x , y , and z positions of source points in the others three columns:

$$\mathbf{P} = \begin{pmatrix} 1 & x_{k_1}^0 & y_{k_1}^0 & z_{k_1}^0 \\ 1 & x_{k_2}^0 & y_{k_2}^0 & z_{k_2}^0 \\ \vdots & \vdots & \vdots & \vdots \\ 1 & x_{k_N}^0 & y_{k_N}^0 & z_{k_N}^0 \end{pmatrix}$$

Radial basis interpolation works for scalar fields. For the smoothing problem, each component of the displacement field prescribed at the source points is interpolated as follows:

$$\begin{cases} v_x = s_x(\mathbf{x}) = \sum_{i=1}^N \gamma_i^x \phi(\|\mathbf{x} - \mathbf{x}_{k_i}\|) + \beta_1^x + \beta_2^x x + \beta_3^x y + \beta_4^x z \\ v_y = s_y(\mathbf{x}) = \sum_{i=1}^N \gamma_i^y \phi(\|\mathbf{x} - \mathbf{x}_{k_i}\|) + \beta_1^y + \beta_2^y x + \beta_3^y y + \beta_4^y z \\ v_z = s_z(\mathbf{x}) = \sum_{i=1}^N \gamma_i^z \phi(\|\mathbf{x} - \mathbf{x}_{k_i}\|) + \beta_1^z + \beta_2^z x + \beta_3^z y + \beta_4^z z \end{cases}$$

The radial basis method has several advantages that make it very attractive in the area of mesh smoothing. The key point is that, being a meshless method, only grid points are moved, regardless of the element connected, and it is suitable for parallel implementation. In fact, once the solution is known and shared in the memory of each calculation node of the cluster, each partition has the ability to smooth its nodes without taking care of what happens outside because the smoother is a global point function and the continuity at interfaces is implicitly guaranteed.

III. Test Case Description

The developed procedure has been applied to the static aeroelastic analysis of the wind-tunnel model of a business-class aircraft in complete configuration (wing, fuselage, engine nacelle, and vertical and horizontal tails). The geometry refers to a wind-tunnel test campaign performed by Piaggio Aero Industries in the ONERA S2MA transonic facility. The model is steel-made and is mounted on a six-component balance (Fig. 1). It is equipped with eight external and four cavity static pressure taps. The flowthrough nacelles have been dimensioned in order to maintain the real engine mass flow rate in cruising condition. The pressure distribution on the surface has been measured using pressure-sensitive paint (PSP) [13]. The ONERA PSP technology is based on the response of a two-component photoluminescent paint excited with UV light. One of the two components of the paint is emitting a blue light, whereas the other one is emitting a red light. The response of the blue component depends on the local oxygen concentration in the air (i.e., the local static pressure) and on the intensity of the UV light excitation. The response of the red component only depends on the intensity of the excitation. A camera takes two consecutive pictures of the painted surface: the first one through a blue filter and the second one through a red filter. The ratio of these two pictures, referenced by the same ratio obtained wind off, is the image of the static pressure field. The external pressure taps, located on the right wing, are used to calibrate the PSP-based measurement procedure.

The Mach number, angle of attack, and drag measurements were systematically corrected for upwash, wind-tunnel calibration, walls, sting line, and fuselage cavity pressure in order to obtain the aircraft data in free-flight condition. The transition was tripped, applying carborundum grains at 5% of the local chord on both sides of the wings, tail, pylons, and nose. The turbulent transition was verified

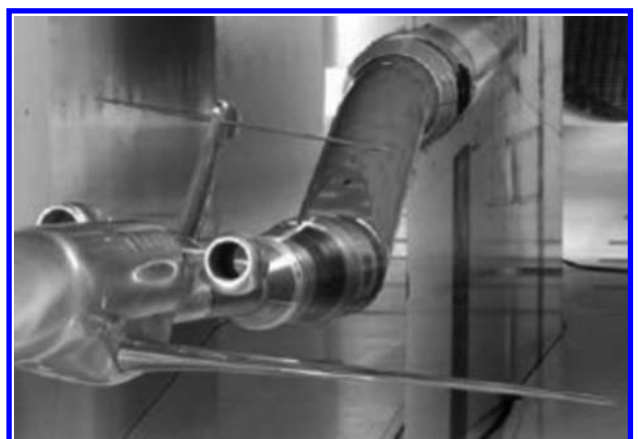


Fig. 1 Wind-tunnel model installation.

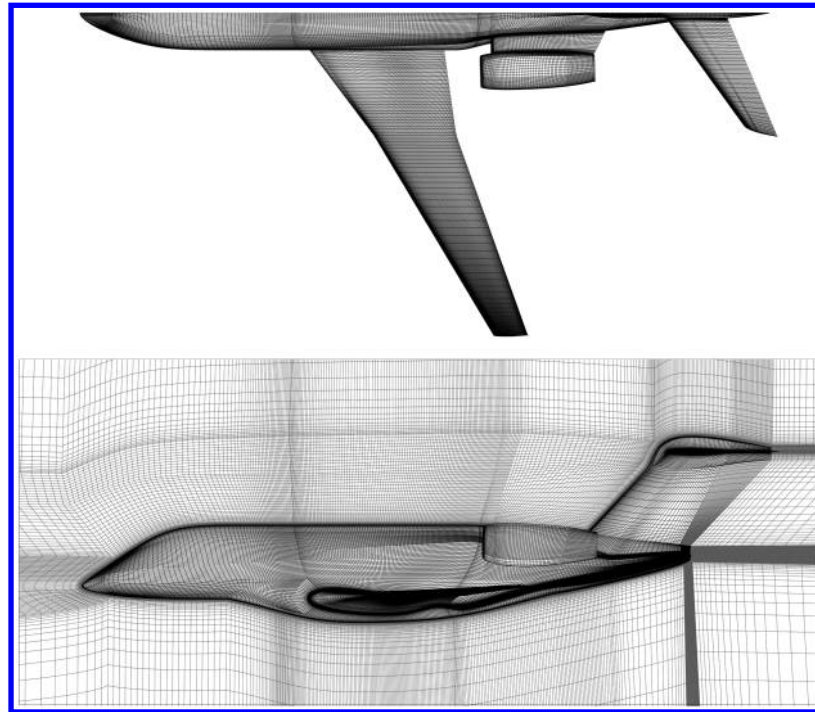


Fig. 2 CFD computational grid detail.

with acenaphtene visualizations. The geometric deformation of the model under load was not measured.

IV. Aerodynamic Analysis

Free-flight conditions were numerically simulated. The computational domain has been generated using ANSYS ICEM/CFD. It is a multiblock (867 blocks) structured hexahedral grid with far field located at around 30 mean aerodynamic chords from the model. All the surfaces are viscous, and the boundary layer is solved up to the wall. The O-grid structure was generated around all the walls, and the cells were clustered in order to keep a Y^+ between 0.5 and 1. The wall normal cell dimension growth rate is lower than 1.3. The elements around the airfoil are 220 and 110 spanwise (Fig. 2). The grid is composed of 14 million cells.

The computations were performed using CFD++, which is a multipurpose commercial CFD software suite [14]. Steady compressible Reynolds-averaged Navier–Stokes computations in double precision using an implicit time integration scheme and a second-order spatial discretization were performed. The wind-tunnel static pressure, temperature, and velocity were imposed at far field. Backpressure was imposed at the domain outlet and adiabatic viscous wall boundary condition on the model surfaces. The flight conditions were Mach 0.8, Reynolds $4 \cdot 10^6$, and 1.4 deg of incidence. The experimental angle of incidence, at which the PSP measurements are referred, is 1.69 deg. The angle used in the computations was tuned in order to match the numerical upper nose pressure distribution, in the inner region of the wing, with the experimental values. Two turbulence models have been tested: the two equation realizable $k-\varepsilon$, which is one of a most common model

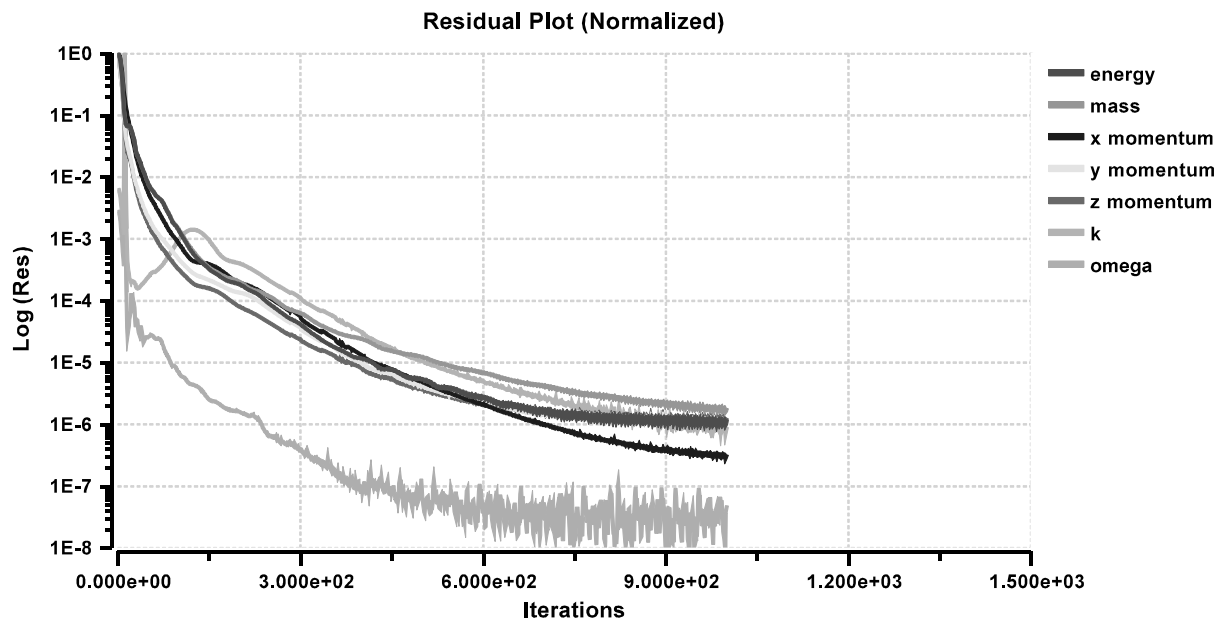


Fig. 3 CFD convergence history.

used for high Reynolds applications; and the Menter $k-\omega$ shear stress transport (SST) model, which was expressly developed for aeronautical applications, adapting its coefficients in the boundary layer with the aim to improve the accuracy on the wall solutions. The first model solves two additional transport equations for the turbulent kinetic energy k and the turbulent dissipation rate ε , while the second solves one equation for k and one for the specific dissipation rate ω [15]. Figure 3 reports the typical convergence history.

V. Finite Element Method Analysis

Figure 4 details the wind-tunnel model structure. The wing root extends into the belly fairing and is bolted to the central balance block. Because of the higher stiffness of the wing root, bolts, and balance structure, in comparison with the external wing, the model deformation is assumed to be limited to the exposed part of the wing. The structural model is then limited to this region, and it is constrained at the wing/fuselage junction.

The wing is full steel made, and the mesh is composed by solid elements in all the wing volume, which is filled with hexacells (Fig. 5). The total FEM model dimension is 28,000 elements. The load is applied on the model using a PATRAN interpolating module starting from the input pressure distribution obtained by the CFD calculation.

VI. Mesh Morphing Method

The updating of CFD mesh can be easily performed using RBF mesh morphing. The RBF-Morph software has been used. Considering that, currently, the tool is available as an add-on for Fluent, the present test has been completed with the aid of Fluent interface. Nevertheless, a standalone library is already available and could be used in future applications to fully automate the method without the need of Fluent software installed.

RBF-Morph allows us to define an arbitrary number of source points in the space. A displacement field that exactly interpolates the value prescribed at each source points is calculated during the fit stage and is available during node updating operation (smoothing) as a closed-form solution. This means that the method is meshless and can be used in parallel and with every kind of mesh element. The most critical point is that the fit is very expensive, especially for large problems where several source points are included in the calculation.

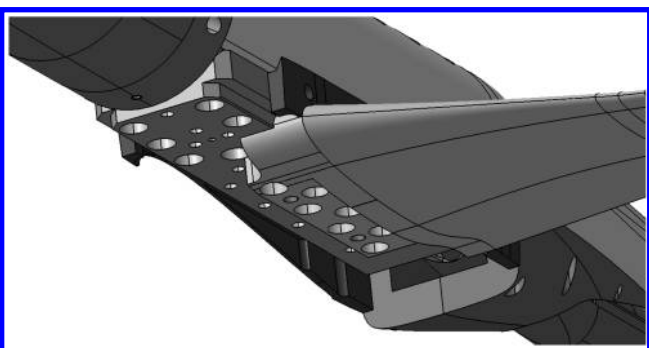


Fig. 4 Detail of wind-tunnel model structure.

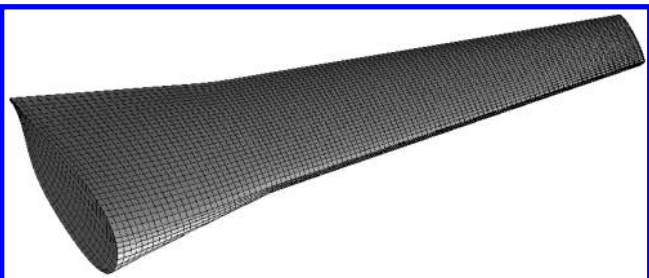


Fig. 5 Wing FEM model.

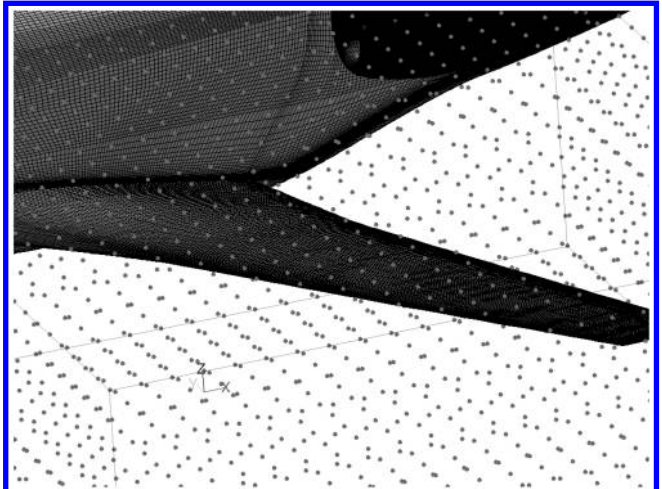


Fig. 6 Box-shaped domain used to define a set of RBF points that prescribe a zero solution and limit the action of the smoother.

The wing movement can be imposed using a box to limit the action of the morpher (and so the complexity of the test) or using all the points on the surfaces, morphing all the volume mesh.

Both methods are explored in order to cope with the most resources demanding approach (that, for this particular application, is well beyond the morphing need but is comparable with the method presented in [1]), and with an optimal approach that, thanks to the domain functionality of RBF-Morph allows us to operate on a small part of the mesh without the need of a clipping of original data, works directly on the full model. In both cases, a two-step approach has been considered. During the first step, FEM node positions and resulting displacements are used to generate a small RBF problem thanks to an automatic tool that allows us to extract information from .BDF and .PCH files (the .BDF file is the standard input file for the Nastran solver, and the .PCH file is a standard output of the Nastran solver that contains FEM problem solution). The obtained solution can be used in the second step (the smoothing one), where the FEM solution is prescribed to all CFD nodes on the wing and a zero movement is prescribed to the remaining nodes on the boundary.

Considering that the setup of the global approach is straightforward because all nodes on the surfaces are prescribed as source points, only the box approach is described in detail. The box is defined using the graphical user interface of RBF-Morph by means of the autostep function that allows us to wrap a set of surfaces (the wing in this case) with a box. The dimension of such a box are then symmetrically adjusted in the plane XZ of the airfoil profile and then in the Z direction (in this case, the box dimension is increased only in the direction of the wingtip). The point spacing is defined in order to have enough zero points on the box boundary that is used as the limit

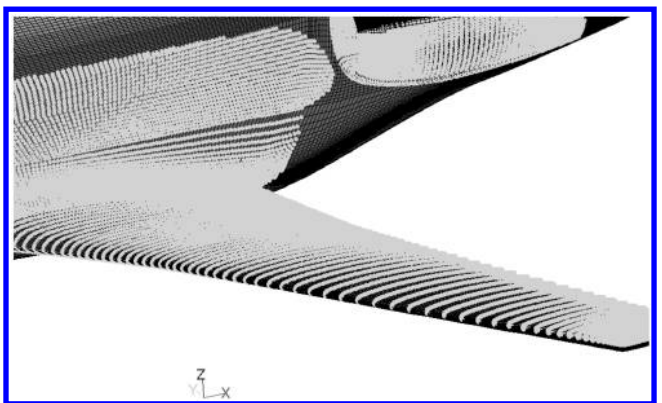


Fig. 7 Preview of surface points. Two sets of surfaces are used: the first to prescribe the FEM solution (interpolated with a previously fitted RBF solution) to all the nodes that belong to the wing, and the second to constrain all the nodes on the aircraft included in the box domain.

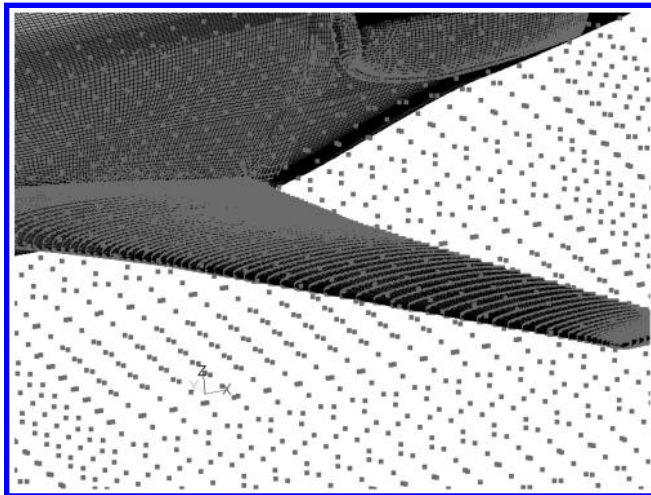


Fig. 8 Complete RBF problem used for the fitting stage.

of the morphing action; the box and generated RBF points are represented in Fig. 6.

All the surfaces of the aircraft and the symmetry plane are then selected using two sets. The first set contains the nodes on the wing, and the second one contains the nodes on the other surfaces. For the node on the wing, the RBF solution obtained using the FEM solution is prescribed, and for the other one, a zero movement is prescribed. The preview of point movements on surfaces is represented in Fig. 7.

The complete set of source points used for the calculation is represented in Fig. 8.

Using the complete boundary (i.e., all the aircraft and the far field), a huge RBF problem composed of 427,944 RBF points needs to be fitted. Such a fitting operation requires 1337 s running on a quadcore Intel i5, 2.67 GHz, with 8 GB. The smoothing stage in this case is very expensive (5445 s), because each CFD node is smoothed using a very large RBF source point data set; usually this stage is performed in parallel and scales proportionally with the number of processors.

Using the box, a smaller RBF problem needs to be fitted (59,729 points) that takes 53 s; the smoothing of the complete CFD mesh takes, in this case, 209 s.

A preview of morphing action on the wing and on a cutting plane is represented in Figs. 9 and 10.

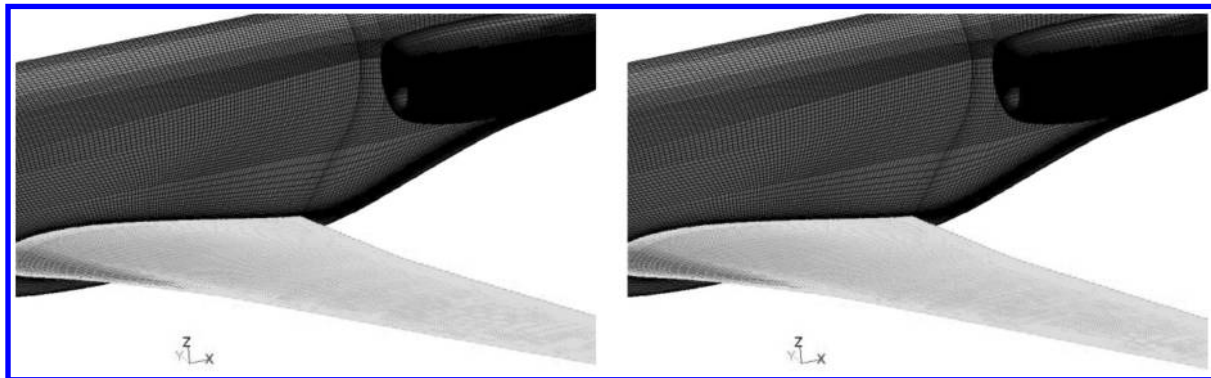


Fig. 9 Preview of wing model deformation.

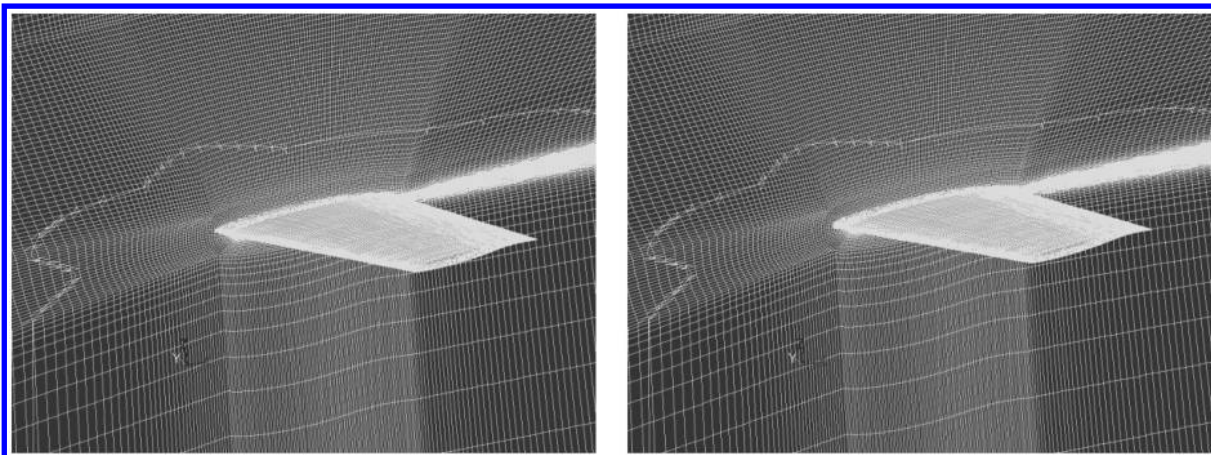


Fig. 10 Preview of wing model deformation on a cutting plane.

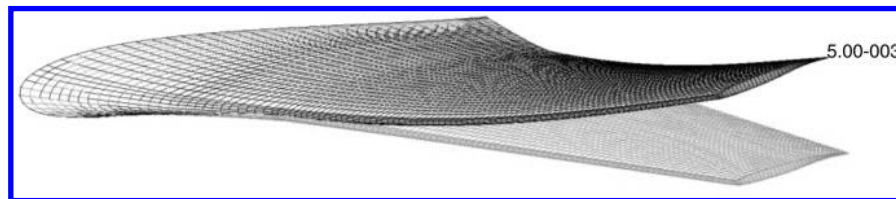


Fig. 11 Wing model deformation.

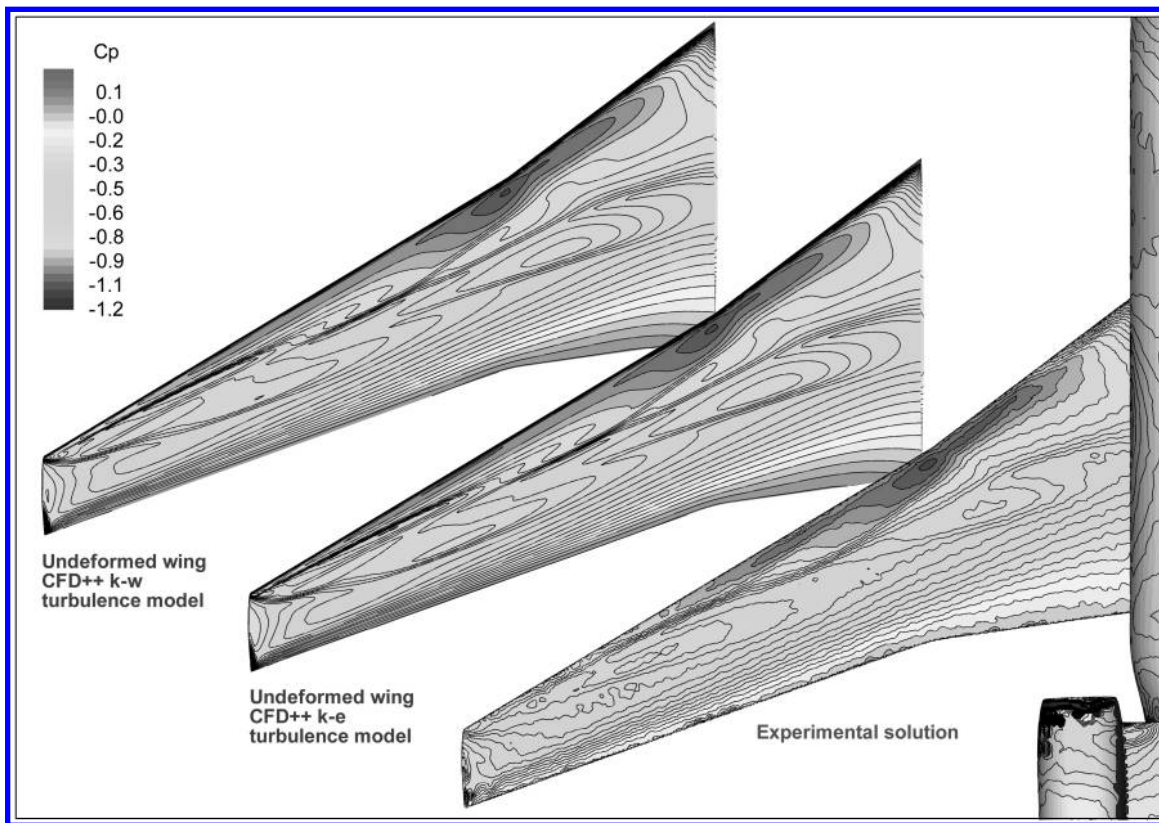


Fig. 12 Comparison between experimental and CFD pressure distributions on undeformed wing.

VII. Results

The model span is 0.6 m. Under aerodynamic loads, the wingtip moves 5 mm from the undeformed geometry. The aerodynamic effect due to the positive sweep angle is a pitching twist increment in the order of a half-degree. Figure 11 compares the

unloaded geometry with the deformed wing, emphasizing the displacements.

Figures 12 and 13 report the measured and the computed pressure distributions on the wing surface for the two tested $k-\varepsilon$ and SST turbulence models obtained on both the undeformed and the

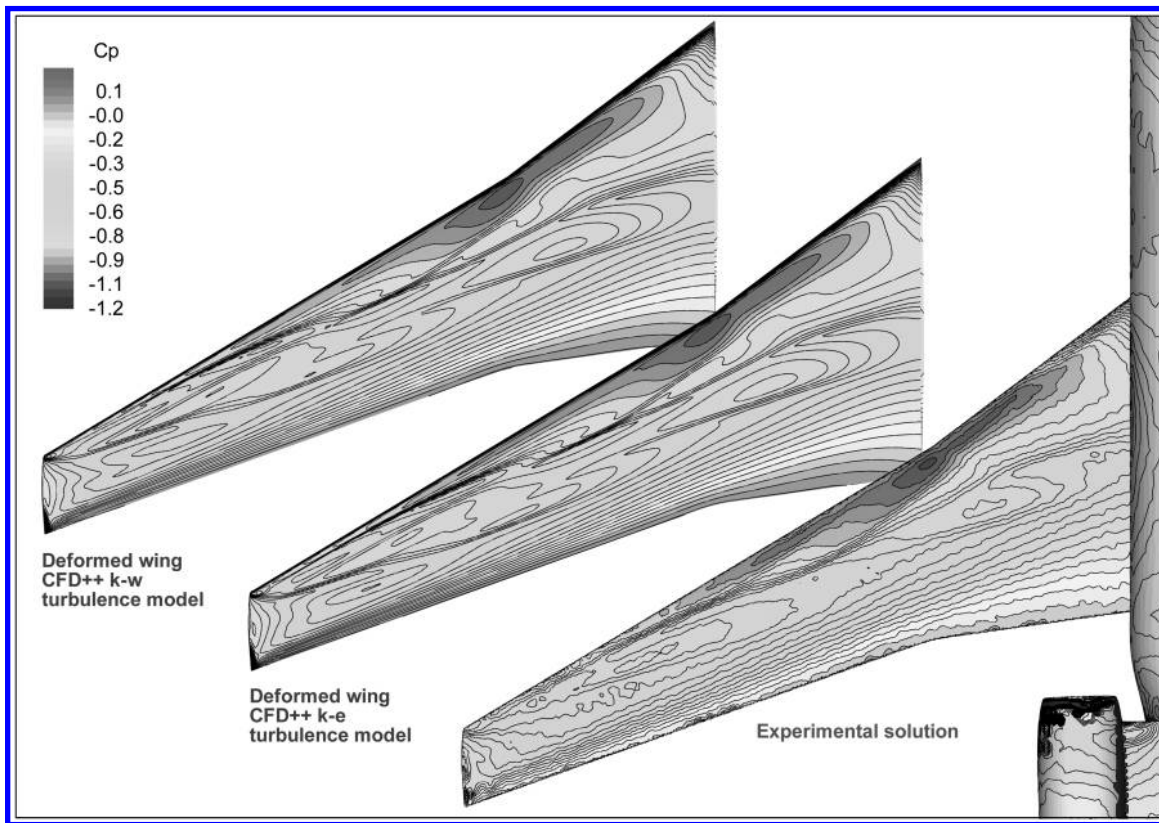


Fig. 13 Comparison between experimental and CFD pressure distributions on deformed wing.

deformed geometries. As expected, the deformation is aerodynamically significant only in the outer region. Here, the computed pressure distribution on the deformed wing better matches the experimental values, particularly in term of shock strengths and position. From Figs. 14–17, the pressure distribution comparison is detailed at four wing sections. The two turbulence models gave a very similar pressure distribution. Small differences appear in the recompression regions where the realizable $k-\varepsilon$ model seems to

predict slightly stronger shocks located more aft than the $k-\omega$ SST model.

Very good agreement is obtained in all sections in most parts of the flexible upper wing surface, with some differences in the waviness evidenced at the most outer section. A disagreement is evaluated in the pressure recovery value at the wing trailing edge.

The pressures do not exactly match the experimental values in the lower surfaces. In the pressure decreasing region, the values are

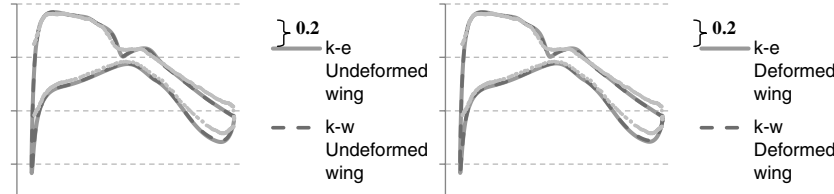


Fig. 14 Detail of pressure solutions at section $y/b = 0.18$.

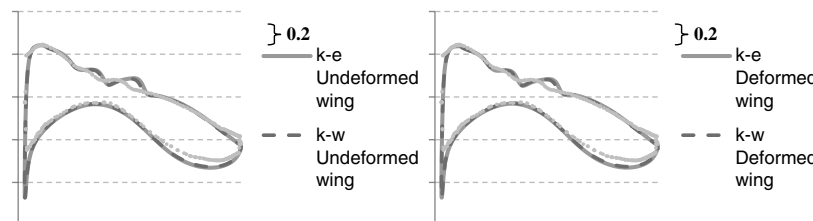


Fig. 15 Detail of pressure solutions at section $y/b = 0.38$.

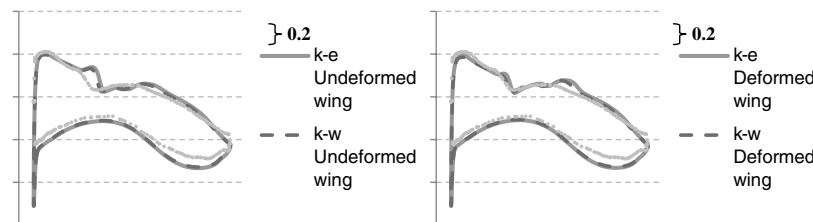


Fig. 16 Detail of pressure solutions at section $y/b = 0.58$.

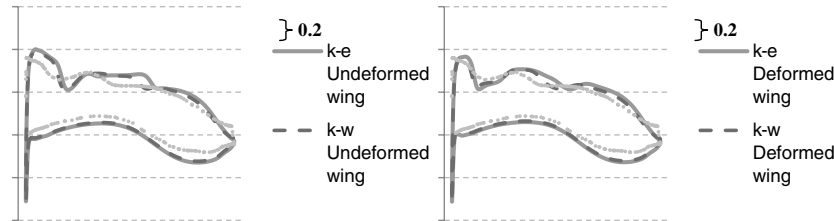


Fig. 17 Detail of pressure solutions at section $y/b = 0.79$.

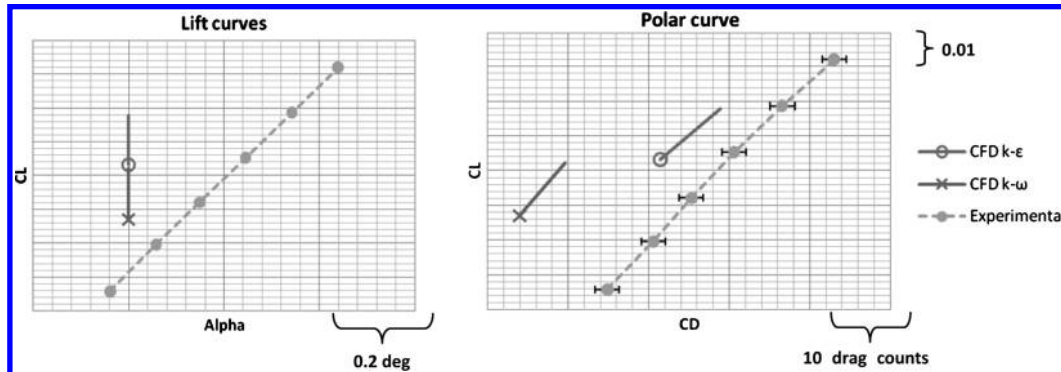


Fig. 18 Comparison between experimental and CFD integral values (marker at deformed wing solution).

slightly uniformly overestimated. This might be due to the wall blockage and to the wind-tunnel incidence correction method, which estimate a slightly higher incidence than in free air. This difference is, however, negligible at a section $y/b = 0.38$ (Fig. 15). The differences become stronger in the recovery region, where a significantly higher load is computed. The direct consequence of this disagreement is an overestimation of the lift coefficient, as clearly evidenced when comparing the experimental lift polar with the numerical solutions (Fig. 18). The reason for this difference is not clear, and further investigations are required. In Fig. 18, the solid lines start from the values obtained on the undeformed geometry and terminate with a marker at the value obtained on the flexible wing. Both turbulence models overestimate the lift and underpredict the drag. As mentioned, the lift disagreement is affected by the uncertainty on the effective incidence and by the overload estimation on the rear lower region of the wing. The drag is better estimated by the $k-\varepsilon$ turbulence model. Its underestimation is around the weight drag counts, while the $k-\omega$ model underestimation is 19 drag counts.

VIII. Conclusions

A static aeroelastic CFD-CSM coupled procedure using high-fidelity methods has been set up and validated. The method is based on the coupling of the aerodynamic and structural analyses through a mesh morphing deformation tool based on RBFs. The procedure has been successfully applied to the analysis of a full aircraft in high-speed cruise configuration. The pressure distribution and the integral coefficients have been compared with the Piaggio Aero Industries proprietary experimental measurement obtained in the ONERA S2MA transonic wind tunnel. The numerical solutions on the flexible wing showed good agreement with the experimental pressure values in most of the wing surface. Some unclear discrepancies have been evaluated in the pressure recovery region of the lower wing surface, which led to a total lift overestimation. The performance of the realizable $k-\varepsilon$ and the $k-\omega$ SST turbulence models have been compared. The first underestimates the drag by eight drag counts, while the latter overestimation is around 19 drag counts. The procedure was shown to be effective and is suitable to be automated for inclusion in a numerical optimization procedure of a flexible object. Further activity is, however, required in order to speed up the communication process between the several codes and to release the mesh morphing method dependency from the software to be used.

Acknowledgment

The work presented in this paper is the result of a cooperative activity between Piaggio Aero Industries and the University of Rome “Tor Vergata”.

References

- [1] Keye, S., “Fluid–Structure Coupled Analysis of a Transport Aircraft and Comparison to Flight Data,” 39th AIAA Fluid Dynamics Conference, AIAA Paper 2009-4198, 2009.
- [2] Jakobsson, S., and Amoignon, O., “Mesh Deformation Using Radial Basis Functions for Gradient Based Aerodynamic Shape Optimization,” *Computers and Fluids*, Vol. 36, No. 6, July 2007, pp. 1119–1136.
doi:10.1016/j.compfluid.2006.11.002
- [3] de Boer, A., van der Schoot, M. S., and Bijl, H., “Mesh Deformation Based on Radial Basis Function Interpolation,” *Computers and Structures*, Vol. 85, Nos. 11–14, June–July 2007, pp. 784–795.
doi:10.1016/j.compstruc.2007.01.013
- [4] van Zuijlen, A. H., de Boer, A., and Bijl, H., “Higher-Order Time Integration Through Smooth Mesh Deformation for 3-D Fluid–Structure Interaction Simulations,” *Journal of Computational Physics*, Vol. 224, 2007, pp. 414–430.
doi:10.1016/j.jcp.2007.03.024
- [5] Baudille, R., and Biancolini, M. E., “FSI Makes FLUENT More Flexible,” *Fluent News*, Vol. 14, Spring 2005, Fluent, Inc., Lebanon, NH, 2005.
- [6] Baudille, R., and Biancolini, M. E., “A General Approach for Studying the Motion of a Cantilever Beam Interacting with a 2-D Fluid Flow,” *Interaction and Multiscale Mechanics*, Vol. 1, No. 4, 2008.
- [7] Baudille, R., and Biancolini, M. E., “Modelling FSI Problems in FLUENT: A General Purpose Approach by Means of UDF Programming,” *FISITA 2006 World Automotive Congress* [CD-ROM], Soc. of Automotive Engineers of Japan, Tokyo, Oct. 2006.
- [8] Angeletti, A., Biancolini, M. E., Costa, E., and Urbinati, M., “Optimisation of Reed Valves Dynamics by Means of Fluid Structure Interaction,” *Simulation for Innovative Design: Proceedings of the 4th European Automotive Simulation Conference*, Munich, edited by K. W. Seibert and M. Jirka, ANSYS, Canonsburg, PA, July 2009, pp. 175–185.
- [9] Biancolini, M. E., Biancolini, C., Costa, E., Gattamelata, D., and Valentini, P. P., “Industrial Application of the Meshless Morpher RBF Morph to a Motorbike Windshield Optimisation,” *Simulation for Innovative Design: Proceedings of the 4th European Automotive Simulation Conference*, Munich, ANSYS, Canonsburg, PA, July 2009, pp. 71–83.
- [10] Biancolini, M. E., “Mesh Morphing Accelerates Design Optimization,” *ANSYS Advantage*, Vol. 4, No 1, 2010.
- [11] Biancolini, M. E., “Mesh Morphing and Smoothing by Means of Radial Basis Functions (RBF): A Practical Example Using Fluent and RBF Morph,” *Handbook of Research on Computational Science and Engineering: Theory and Practice*, IGI Global, (in press).
- [12] Biancolini, M. E., and Celli, U., “An Advanced RBF Morph Application: Coupled CFD-CSM Aeroelastic Analysis of a Full Aircraft Model and Comparison to Experimental Data,” *Low Carbon Vehicles: Proceedings of the 8th MIRA International Vehicle Aerodynamics Conference*, Oxford, MIRA, Warwickshire, England, U.K., Oct. 2010, pp. 243–258.
- [13] Le Sant, Y., “Overview of the Self-Illumination Effect Applied to Pressure Sensitive Paint Applications,” *Instrumentation in Aerospace Simulation Facilities, 2001: 19th International Congress on ICIASF 2001*, IEEE Publ., Piscataway, NJ, Aug. 2001, pp. 159–170.
- [14] “CFD++ User Manual,” Metacomp Technologies, Inc., Agoura Hills, CA, 2010.
- [15] Menter, F. R., “Two-Equation Eddy-Viscosity Turbulence Models for Engineering Applications,” *AIAA Journal*, Vol. 32, No. 8, 1994, pp. 1598–1605.
doi:10.2514/3.12149